Frontal rainfall observation by a commercial microwave communication network

Artem Zinevich
Hagit Messer
Pinhas Alpert
Tel Aviv University, Israel

Corresponding author address: Artem Zinevich, The Porter School of Environmental Studies, Tel Aviv University, Ramat Aviv, Tel Aviv, Israel, 69978
E-mail: artemsin@post.tau.ac.il

ABSTRACT

A novel approach for reconstruction of rainfall spatial-temporal dynamics from a wireless microwave network is presented. It employs a stochastic space-time model based on a rainfall advection model, assimilated using a Kalman filter. The technique is able to aggregate the data in time and space along the direction of motion of the rainfall field, which is recovered from the simultaneous observation of a multitude of microwave links.

The technique is applied on a standard microwave communication network used by cellular communication system and comprising 23 microwave links, and it allows observation of near-surface rainfall at the temporal resolutions of 1 minute. The accuracy of the method is demonstrated by comparing instantaneous rainfall estimates with measurements from five rain gauges, reaching correlations of up to 0.85 at 1 minute time interval with bias and RMSE of -0.2 mm h^{-1} and 4.2 mm h^{-1} respectively, and up to 0.96 with RMSE of 1.6 mm h^{-1} at the 10 minutes time interval, for a 22-hour intensive rainstorm with average rain rate of 3.0 mm h^{-1} and peak rain rate of 84 mm h^{-1}. The results are compared to those of other spatial reconstruction techniques.

The proposed dynamic rainfall reconstruction approach can be applied to larger scale dynamic rainfall assimilation methods, enabling interpolation over data-void regions and straightforward incorporation of data from other sources, e.g. rain gauge networks and radars.

1. Introduction

Accurate measurements of rainfall intensity are critical for numerous applications, ranging from flood warnings, urban drainage planning and fresh water resource management playing a vital role in many parts of the world, to global circulation and climate analysis.

It has long been known that the attenuation A [dB km^{-1}] of a radio signal at the frequencies of tens GHz is dominated by the effects of rainfall R [mm h^{-1}] and is governed by a well-known power law equation:

$$A = aR^b \quad (1)$$

where the parameters a and b are, in general, functions of link frequency, polarization and drop size distribution (DSD), see Jameson (1991). Microwave links can therefore serve as a basis for measurements of path-integrated and area-integrated rainfall (Atlas and Ulbrich 1974, 1977). The advantage of microwave links for high temporal resolution measurements over conventional rain gauges was demonstrated by Minda and Nakamura (2005).

Recent advances in wireless communication technology bring about the opportunity of using commercial microwave communication hardware, available off-the-shelf. The use of dual-frequency microwave links, operating on different, specially selected frequencies, allows producing reliable estimates of path-integrated rainfall (Holt et al. 2000; Rahimi et al. 2003) and rainfall spatial distribution, in conjunction with rain-gauges and radar (Grum et al. 2005). A number of applications of dual-frequency microwave measurements were explored: calibration of weather radar (Rahimi et al.

2006), correction of X-band radar rainfall estimates (Krämer et al. 2005) , identification of melting snow (Upton et al. 2007) and even estimation of DSD parameters (Rincon and Lang 2002). The potential of use of single-frequency links for urban rainfall measurements was revealed by Upton et al. (2005).

The use of microwave attenuation measurements for the tomographic reconstruction of rainfall fields was pioneered by Giuli et al. (1999) who suggested a specially designed hypothesized system of microwave links with predefined geometry, operating at either specially selected frequencies where the $A - R$ relationship is linear or using differential phase shift, combined with point rain gauges. This system allowed application of linear tomography to reconstruct spatial distribution of rainfall. All of these approaches, however, rely on dedicated, specially installed equipment.

The feasibility of cost-free estimation of near-the-ground rainfall from attenuation measurements in standard commercial microwave networks was demonstrated by Messer et al. (2006) and Leijnse et al. (2007a). The use of commercial hardware installations poses new challenges, because commercial microwave networks are optimized for high communication performance and are designed in the way that reduces the effect of weather-related impairments on quality of service. Thus, the observation type, time and magnitude resolution, network geometry and frequencies are predefined and, in most cases, cannot be changed; records of received signal level (RSL) are distorted by quantization. Other difficulties in estimation of average rainfall per link from signal attenuation include uncertainties due to variability of DSD along the link (Berne and Uijlenhoet 2007), wet antenna attenuation (Minda and Nakamura 2005; Leijnse et al.

2008) and uncertainty in determination of clear air attenuation due to water vapor-induced attenuation and scintillation effects (Holt et al. 2003; Rahimi et al. 2003).

Tomographic reconstruction of spatial rainfall intensity distribution from RSL records in commercial microwave networks is addressed by Goldshtein et al. (2008) and Zinevich et al. (2008).

In this paper it is demonstrated how the RSL records from standard microwave communication equipment can be applied for reconstruction of rainfall dynamics at the temporal resolution of 1 minute. The studied event is a 22-hours strong rainstorm (a cold front movement) on 26-27 December 2006 with a peak intensity reaching 84 mm h^{-1} (extrapolated from 1-minute rainfall value), comprising a sequence of continuous strips of cumulonimbus clouds, preceding the cold air mass and moving southeastwards (Figure 1). This convective rain cloud system is typical for mid-winter in Israel and is characterized by continuous precipitation with higher rainfall intensity at its leading edge (Goldreich 2003).

This event has been studied using data collected by an operating star topology network of 23 microwave links from an Israeli cellular provider; all are vertically polarized and are transmitting at the frequency bands of 18, 22 and 23 GHz. The transmitter-receiver separation distance varies from 0.8 to 18 km; the network operates in the cities of Ramle and Modi'in in Central Israel, covering an area of 32x25 km^2. The built-in measurement and logging facilities register RSL at the magnitude resolution of 1 dB every minute. The rainfall estimates were compared to the measurements of five tipping-bucket rain gauges (Figure 2) with tipping volume of 0.1 mm and the resolution of tipping time registration of 1 min^{-1}, providing the magnitude quantization of 6 mm h^{-1}.

Even over this limited area, the density of the links varies considerably, reaching its highest around Switch Ramle in the middle of Ramle city. East to Ramle, however, the representativeness is rather poor, which is a natural consequence of the fact that the density of cellular masts often follows that of the population and is low in suburban areas.

To fill the gaps between links, a stochastic spatio-temporal model was employed. This model is able to aggregate the data in time and space along the direction of motion of the rainfall field, based on the advection model. It describes the evolution of the rain field in time, assuming that during short time periods (minutes), the main force acting on a rain cell is advection. The transport model uses the estimates of local rainstorm velocity and direction derived from the analyses of correlation of rainfall peaks among the links. The estimation of hidden variables (spatial distribution of rainfall), along the direction of motion is done using a non-linear Extended Kalman filter (EKF) over the system of links, producing the instantaneous reconstructed rainfall fields over a Cartesian grid. In addition, the estimates of the proposed dynamic reconstruction approach were compared with those of two other spatial reconstruction techniques.

The proposed dynamic rainfall approach can be adopted to larger scale assimilation systems, enabling interpolation over data-void regions and straightforward incorporation of data from other sources – rain gauge networks and radars, similarly to the algorithm demonstrated by Grum et al. (2005). The technique can find applications in thunderstorm nowcasting, where accurate measuring of precipitation and rainstorm dynamics with sufficient time and space resolution is essential (Wilson et al. 1998).

The paper is organized as follows. In section 2, the space-time model is described. In section 3 the use of the EKF is detailed, and section 4 describes the estimation of the storm dynamics. Section 5 outlines the spatial reconstruction and in section 6 a specific case study is analyzed. Section 7 concludes the paper.

2. Space-time model

The advection equation is the one describing the transport of a conserved scalar quantity in a vector field. Advection often refers to the transport of some property of the atmosphere or ocean, such as heat, humidity or chemical constituents. It is widely used in meteorology and atmospheric studies (Allen *et al,* 1991; Daley 1995).

The use of an advection-diffusion model to describe the evolution of rainfall in space and time, aimed for real-time prediction of rainfall distributions and forming a stochastic framework in which both rain gauge and radar data may be included, has been considered by several authors (see, for example, Mizutani 1981; Jinno et al. 1993; Kawamura et al. 1997). The latter proposed a method, based on a two-dimensional stochastic advection-diffusion equation including a development/decay term in combination with a Fourier domain shape method. It was shown that the model can forecast motion, shape, size and intensity distribution of individual rain cells, using a Lagrangian view of the rainfall intensity field. Note that such model should not be considered as an attempt to physically model the turbulent and thermodynamic behavior of convective air but just a convenient way to describe the rainfall dynamics as observed at the ground level.

Since the present study is oriented on estimation of an arbitrary rainfall field from microwave links rather than temporal evolution of behavior of a single rain cell as in Kawamura et al. (1997), this model was employed in the Eulerian view. In this case, however, estimation of the diffusion and, especially, the development/decay coefficients in every point in space would require observation redundancy that is absent in the relatively sparse network under study; the model was therefore reduced to the pure translation. The basic assumption of such a model is that the rainfall intensity distribution can be considered as a conserved quantity over a short time interval (a few minutes), relatively to the typical lifetime of a rain cell (about an hour in Israeli climate); advection is assumed to follow isobaric surfaces and is therefore predominantly horizontal. The dynamically propagated estimates of rainfall spatial distribution are then corrected with EKF according to the newly observed data.

In the spatial dimension, the wind vector field (*U,V*) at the steering level of a storm is considered curl-less and divergence-less over a small area (32x25 km^2) with simple topography, and changing slowly over the interval of 3 hours, which is a plausible assumption for the cold front convective rainfall in synoptic systems. Even though the advection model does not require this assumption, it is necessary to estimate the wind field aloft from the microwave observations. Note that even within the same climatic region, these assumptions can be invalid for other seasons and types of rainfall storms.

In contrast to Kawamura et al. (1997), here the model is implemented in spatial domain, where efficient numerical schemes exist. The two-dimensional advection equation is integrated for a volume element, and thus a finite-volume scheme for a regular grid $M_y \times M_x$ is obtained (h is equal to ½):

$$r_{i,j}^{t+1|t} = r_{i,j}^{t} + F_{i,j-h}^{t} - F_{i,j+h}^{t} + G_{i-h,j}^{t} - G_{i+h,j}^{t} \quad (2)$$

Here, $r_{i,j}^{t}$ equals rainfall intensity in the (i,j) pixel center, $i = 1,\ldots,M_y$, $j = 1,\ldots,M_x$ at time *t* and $F_{i,j\pm h}^{t}$, $G_{i\pm h,j}^{t}$ are fluxes across boundaries of (*i, i±1)* and *(j, j±1)*.

$r_{i,j}^{t+1|t}$ stands for predicted rainfall intensity of $r_{i,j}^{t+1}$ based on the estimations at time *t*, without accounting for observations at time *t+1*. This will be used later in the EKF formulation.

There is a variety of possible numerical schemes for estimation of fluxes *F* and *G* (e.g. Hourdin et al. 1999). In the present experiments, the form based on the van Leer scheme described by Allen et al. (1991) was used, where not only rainfall intensities in box centers but also their spatial gradients (slopes) are taken into account (this is essential to counteract the numerical diffusion):

$$F_{i,j-h}^{t} = u_{i,j-h}^{t} \begin{cases} r_{i,j-1}^{t} + 0.5\left(1 - u_{i,j-h}^{t}\right)\Delta_{j-1}^{t} r_i, & u_{i,j-h}^{t} \geq 0 \\ r_{i,j}^{t} - 0.5\left(1 + u_{i,j-h}^{t}\right)\Delta_{j}^{t} r_i, & otherwise \end{cases} \quad (3)$$

Here, the dimensionless advection velocity $u_{i,j-h}^{t} = U_{i,j-h}^{t}\,\Delta t/\Delta x$ in the x direction is the local Courant number of the flow, which absolute value should be less than one for the numerical stability of the method. The flux $F_{i,j+h}^{t}$ and fluxes $G_{i\pm h,j}^{t}$ due to the second wind component *V* are calculated analogously. The values $\Delta_{j}^{t} r_i$ (and, correspondingly, $\Delta_{i}^{t} r_j$ for the second dimension) are the local slope estimates. A simple expression for Δr which minimizes numerical diffusion and guarantees monotonicity is:

$$\Delta_j r_i = \begin{cases} 2\dfrac{S_{i,j}}{r_{i,j+1} - r_{i,j-1}}, & S_{i,j} = \left(r_{i,j} - r_{i,j-1}\right)\left(r_{i,j+1} - r_{i,j}\right) \geq 0 \\ 0, & otherwise \end{cases} \quad (4)$$

If Δr are set to zero (e.g. in the buckling areas, where the slope estimates is set to zero), the method reduces to simple diffusive upstream differencing (Allen et al. 1991).

The spatial resolution of the system is theoretically limited by the Courant numbers which, in turn, are determined by the advection speed of a storm given the desired Δt. In practice, the model (3) produces numerical artifacts (oscillations due to sharp spatial gradients, typical for high-order schemes) at the resolution of 1x1 km^2, even in cases when Courant numbers u and υ are less than one (that happens at the advection velocity of 17 m s^{-1}, which is quite common). The results presented here are in the scale of 1.5x1.5 km^2. Increasing pixel size does not lead to performance improvement since bigger pixels average over larger areas that smoothes the reconstructed rainfall; this lowers the validity of the assumption of constant rain rate over a pixel.

3. Extended Kalman filter

The Kalman filter (Drécourt, 2004) is an efficient data assimilation method that explicitly accounts for the dynamic propagation of errors in the model. For linear models with known statistics of the system and measurement errors, the Kalman filter provides an optimal estimate of the state of the system, in terms of minimum estimation error covariance, without assuming any specific distribution of model and observation errors, by just requiring error to be zero-mean and uncorrelated in time (Drécourt, 2004). The use of non-linear models requires the extended Kalman filter, where propagation is based on a statistical linearization of the model equation. It should be noted that due to linearization, EKF is not necessarily optimal.

EKF estimates spatial-temporal precipitation distribution $\mathbf{r}^t$ from a set of incomplete (non-uniform and sparse network of backhaul links) and noisy (complicated by quantization noise) observations $\mathbf{o}^t$, combining past predictions with new observations. The state transition model is given by:

$$\mathbf{r}^{t+1} = f\left(\mathbf{r}^{t}, \boldsymbol{\varepsilon}^{t+1}\right) = \mathbf{r}^{t+1|t} + \boldsymbol{\varepsilon}^{t+1} \quad (5)$$

where $\mathbf{r}^{t+1|t}$ is the prediction of the true rainfall $\mathbf{r}^{t+1}$ from the $\mathbf{r}^{t}$ according to the propagation model (2); $\boldsymbol{\varepsilon}^{t+1}$ is a stochastic component – zero-mean noise with a covariance matrix $\mathbf{Q}^{t}$, accounting for the evolution of rainfall field which is not described by the model (2). Note that $f\left(\cdot,\cdot\right)$ is non-linear since it contains the second-order terms used in the calculation of Δr (4); the linearized operator, used in EKF calculations, is given by Jacobian $\mathbf{J}^{t+1} = \partial \mathbf{r}^{t+1|t} / \partial \mathbf{r}^{t} \Big| \mathbf{r}^{t}$.

The observation model $h\left(\cdot,\cdot\right)$ relates the hidden state space $\mathbf{r}$ to the observable space:

$$\mathbf{o}^{t+1} = h\left(\mathbf{r}^{t}, \mathbf{v}^{t+1}\right) = \mathbf{o}^{t+1|t} + \mathbf{v}^{t+1} \quad (6)$$

$$\mathbf{o}^{t+1|t} = \left[A_1^{t+1|t}, \ldots, A_N^{t+1|t}\right]^T \quad (7)$$

Here, $\mathbf{o}^{t+1|t}$ is the predicted microwave attenuation, calculated from the predicted state $\mathbf{r}^{t+1|t}$ and $\mathbf{v}^{t+1}$ is the zero-mean measurement noise with a covariance matrix $\mathbf{R}^{t+1}$, associated with an observation at time *t+1*. The function $h\left(\cdot,\cdot\right)$ is constructed according to the power-law equation (1) over the reconstruction grid of $M_y \times M_x$ blocks (rainfall intensity is assumed to be constant within a block):

$$A_k^{t+1|t} \approx \sum_{i=1}^{M_y} \sum_{i=1}^{M_x} l_{i,j,k} a_k \left(r_{i,j}^{t+1|t}\right)^{b_k}, \; k = 1, \ldots, N \quad (8)$$

where $l_{i,j,k}$ is the length of the *k*th link segment over the grid block $\left(i, j\right)$. The non-linear operator $h\left(\cdot,\cdot\right)$ is linearized for the EKF calculations:

$$\mathbf{H}^{t+1} = \left.\frac{\partial A_k}{\partial r_{i,j}}\right|_{t+1|t} = l_{i,j,k} a_k b_k \left(r_{i,j}\right)^{b_k - 1}\Big|_{t+1|t} \quad (9)$$

Note that for any $b_k < 1$ (for example, for a horizontally-polarized link, operating at high frequencies), the derivative does not exist for $r_{i,j}^{t+1|t} = 0$. To overcome this issue, we constrain $\mathbf{r}^{t+1|t}$ to minimum 0.001 mm h^{-1} at every iteration t. The choice of the constant has little impact on the performance of the algorithm; it just should be small enough to be considered zero rainfall. The rest of the Kalman equations are standard (Drécourt, 2004).

The power-law coefficients a_k and b_k specific for the kth link, $k=1,\ldots,N$ were estimated using the T-matrix method for calculation of the extinction cross section (Mishchenko, 2000) according to the lognormal model of DSD, parameterized by two-years DSD measurements in Israel; it was found by Feingold and Levin (1986) that this model is well suited to Israeli climatology. The resulting values are given in Table 1.

The performance of the formulated EKF model largely depends on accuracy of estimation of the process and measurement covariance matrices **Q** and **R**. The measurement noise $\mathbf{v}$ should, in general, take into account the uncertainties in estimation of the zero rainfall RSL due to atmospheric and instrumental (observation quantization) impairments.

The former is treated in the pre-processing stage. Knowing the exact zero rainfall RSL at every time frame is important to achieve proper estimation of line-integrated rainfall-induced attenuation. The mean zero level was estimated for each link separately over a 5-hour dry period prior to the beginning of the event and then subtracted from the microwave records; the occasional negative values were clipped to zero. The measured rainfall-induced attenuation $\tilde{A}_k^t$, $k=1,...,N$, $t=1,..,T$ was corrected for wet antenna attenuation according to the two-parameters correction function (Leijnse et al., 2007b), modified so that the wet attenuation is independent on link length:

$$A_k^t = \tilde{A}_k^t - \min\begin{cases} C_1\left(1-\exp\left\{-C_2\dfrac{\tilde{A}_k^t}{l_k}\right\}\right) \\ \tilde{A}_k^t \end{cases} \quad (10)$$

The parameters C_1 and C_2 were calibrated by minimizing $\sum_t\left(A_k^t - a_k\left(R^t\right)^{b_k} l_k\right)^2$ between link L11 of the length $l_{11} = 1.60$ km (see Figure 2) and the time series R^t of rainfall records from the Switch Ramle rain gauge for one hour of the event, from 1500 to 1600 LT (Local Time) 26 December 2006. The correction (10) was applied then to all existing microwave links since all microwave antennas used in the study are of the same type and from the same manufacturer; it was shown (Leijnse et al. 2008) that wet antenna attenuation is mostly independent on frequency in the range of 18-23 GHz.

The measurement noise $\mathbf{v}^t$ accounts for the quantization noise that is modeled as an additive uniformly distributed random variable with a covariance matrix:

$$\mathbf{R} = \mathbf{I}\cdot\sigma_q^2 = \mathbf{I}\frac{\Delta^2}{12} \quad (11)$$

where Δ is quantization interval in dB (equal to 1 dB for the microwave network used in this study).

The process noise $\boldsymbol{\varepsilon}^{t+1}$ involves the variations of the precipitation field which are not described by the model (2). In general, the correct way to estimate the process covariance would be collecting enough statistics of the residual $\mathbf{r}^{t+1|t} - \mathbf{r}^{t+1}$ for rainfall patterns, specific for a given region, season and a phase of a rainstorm. However, the microwave observation network, considered in the present study is rather sparse and limited in size. The system needs therefore to be able to quickly adapt to the changes in the storm that are not accounted by (2), for example, an arrival of the rainstorm front into the monitored area (the model is initialized with zero rainfall). For this reason, the uncertainty of the component $\boldsymbol{\varepsilon}$, expressed in the covariance matrix $\mathbf{Q}$, is necessarily high. In practice, the optimal values of $\mathbf{Q}$, obtained from pilot simulations of the EKF model given the experimental setup (Figure 2), exceed that of the measurement noise $\mathbf{v}$ by orders of magnitude; the value of $\mathbf{v}$ lies in optimal weighting of observations from individual links, according to their uncertainty. This fact naturally fits the Kalman framework: in the case when the predicted (model) rainfall is very uncertain due to the undefined (zero) boundary conditions and limited observation area, the optimal (maximum) advantage is taken from the available measurements. The system is therefore weakly sensitive to the assumptions about the model (e.g. pixel size, accuracy of the advection velocity estimation) at the pixels, crossed by microwave links; the accurate modeling remains important for rainfall estimation in the data-void regions.

For this limited and sparse network configuration the white model noise was assumed (the model covariance matrix is diagonal). In order to allow the model to quickly adapt to the arrival of the front, the values $\mathbf{Q}$ on the main diagonal were initialized by the variance of the all non-zero observations from one of the rain gauges (Ramle West) during the rainstorm under investigation, $(\mathbf{Q})_{kk}$ =111 mm^2 h^{-2}, $k = 1,...,M_y \times M_x$, expressing this way the maximum uncertainty about expected rainstorm front arrival. In general, $\mathbf{Q}$ represents the prior information about a rainstorm;

in the studied event, **Q** was estimated from the observations of the rainstorm itself, so that the present study cannot be considered as real-time monitoring. In practice, the values of **Q** can be either taken according to the anticipated rainfall intensities in the storm, or just as an average over the data, observed in the past, representing similar rainfall patterns.

Note that in this case the distribution of the model noise **ε** cannot be considered zero-mean even approximately (it is just the distribution of rain rates in the event). For this reason, posterior covariance estimates were not analyzed in this paper, even though for a wider and denser network and well-calibrated **Q** and **R** it is possible to get estimates of variances of the reconstructed rainfall in any point in space.

4. Estimation of storm dynamics

To estimate the dynamic parameters of the rainstorm (wind velocity and the direction of the storm movement), the vector analyses technique, used by Desa and Niemczynowicz (1997) based on tracking of the arrival time of a prominent feature of the storm and further extended by Upton (2002), was adopted. The time lags $\delta t_{i,j}$, corresponding to delays in arrival of the storm front were taken according to the best cross-correlations $\rho_{i,j}$ between all pairs ($i,j=1,\ldots,N$) of microwave links in the monitored area. Knowing the spatial locations of links which are determined by the coordinates of a link midpoint and taking into account that the plurality of links is arbitrarily oriented in space, one can expect that averaging over a number of link pairs can allow measuring the dynamics of the rainstorm. Note that this assumption of plausibility of approximation of a link as a point for the dynamics analyses is reasonable when the length of a link is smaller than the typical size of a feature (e.g. rain cell). To reduce the effects of local rainfall variation on accuracy of estimation of $\delta t_{i,j}$, the registered time series were passed through a low-pass three-tap FIR filter with 6dB cut-off frequency of $\pi/2$ ($H(z) = 0.25 + 0.5z^{-1} + 0.25z^{-2}$).

One of the problems in such an approach is the identification of the features, corresponding to the same rain cell over time series, recorded by different gauges (microwave links in this study), if more than one rain cell appears in the monitored area. The cross-correlation coefficient $\rho_{i,j}$ was used as a measure of reliability of the estimate $\delta t_{i,j}$, i.e. how likely that the (i, j) time series are produced by the same feature of the rainstorm.

In a three-dimensional space where $\delta x_{i,j}$, $\delta y_{i,j}$ are the projections of the distance between the midpoints of each pair of links (i, j) on the (x, y) axes and δt is the time axis, movement of a rainfall front can be represented as a plane, described by coefficients (p_1, p_2):

$$p_1\delta x_{i,j} + p_2\delta y_{i,j} = \delta t_{i,j} \quad (12)$$

For all pairs of total N links, the system of $\binom{N}{2}$ linear equations is written as:

$$\mathbf{Mp} = \boldsymbol{\delta}\mathbf{t} \quad (13)$$

This system of linear equations is over-determined for $N \geq 3$ and can be solved using the method of weighted least squares, where each equation, corresponding to a pair of links, is weighted by its correlation powered by a parameter $\gamma >> 1$, reducing this way the effect of link pairs with low value of the correlation peak, which most likely do not correspond to the same features of the rainfall field:

$$\mathbf{W} = \begin{bmatrix} \rho_{1,2}^{\gamma} & & \\ & \ddots & \\ & & \rho_{N-1,N}^{\gamma} \end{bmatrix} \quad (14)$$

The parameter γ should be taken sufficiently large so that only observations with the most prominent correlations affect the result. Yet, due to the short length of the time series used in calculations of correlations, outliers which are very common should be removed. The solution is refined by discarding P percents of the equations (most likely outliers), showing the worst mismatch between the measured and estimated correlation lags $\mathbf{\Delta} = |\mathbf{\delta t} - \mathbf{Mp}|$ and then the refined estimate $\tilde{\mathbf{p}}$ is recalculated using (13). This procedure may be repeated several times; in practice, it was found that two iterations is enough (Figure 3).

The refined mean squared mismatch $\left\langle \tilde{\mathbf{\Delta}}^2 \right\rangle = \left\langle (\mathbf{\delta t} - \mathbf{M\tilde{p}})^2 \right\rangle$ can provide an indication of the fit goodness and can be used to estimate the optimal γ ($\langle \cdot \rangle$ denotes the averaging operation). Thus, over the entire event, the optimal $\gamma = 10$ is obtained as $\gamma = \arg\min_{\gamma} \left\langle \tilde{\mathbf{\Delta}}(\gamma)^2 \right\rangle$ (Figure 4, A). On the other hand, large $\left\langle \tilde{\mathbf{\Delta}}^2 \right\rangle$ indicate low confidence of the estimates, i.e. the lack of consistent features registered by majority of microwave links; time frames with $\left\langle \tilde{\mathbf{\Delta}}^2 \right\rangle > \tau$ are invalidated. In the study, the whole 22-hour event was divided into 14 three-hour frames with 1.5 hour overlapping; the distribution of $\left\langle \tilde{\mathbf{\Delta}}^2 \right\rangle$ is shown at Figure 4 (B); the confidence threshold $\tau = 20\ \mathrm{s}^2$ was chosen accordingly. The measured advection slowness $\|\mathbf{p}\|$ and the tangent of direction $d = p_1 p_2^{-1}$ from all confident frames were interpolated then into the 1 minute scale using cubic splines; the advection velocity and direction were finally obtained as

$\| \boldsymbol{\upsilon} \| = \| \mathbf{p} \|^{-1}$ and the arc tangent of *d.*

The value of *P* is in general depends on the network configuration and is determined experimentally; in the present study, it was taken 0.75. The resulting velocity and directions for the event, determined from 23 microwave links for the entire event are plotted at Figure 5.

It is important to note that the suggested approach does not estimate the true wind direction but its component, normal to the front. If the assumption of collinearity of wind direction and the front-normal component does not hold and different parts of the front resemble each other, the advection direction and speed, determined by the method differs from the true wind direction at the steering level of a storm.

5. Spatial reconstruction

To get better insight into the advantages of the proposed spatio-temporal method, we consider as references a stochastic interpolation technique (SHT) by Goldshtein et al. (2008) and a non-linear tomography technique (NLT) by Zinevich et al. (2008) which are briefly outlined below.

a. Stochastic interpolation.

In the stochastic reconstruction, each link $i=1,\dots,N$ of the length l_i is divided into a set of K_i equal intervals, where the rainfall intensity is assumed to be constant, so that the total path attenuation equals $A_i = \sum_{j=1}^{K_i} A_{i,j}$. Each interval is then represented as a sample point with (unknown) rainfall intensity $r_{i,j}$, $i=1,\dots,N$, $j=1,\dots,K_i$, distorted by quantization noise n_i inherited from its parent link. The variance of the quantization noise σ_i^t is approximated by Taylor series expansion of the non-linear function $R_i = R\left(\tilde{A}_i + n_i^A\right)$, where $\tilde{A}_i$ is the true path-integrated rainfall-induced attenuation and n_i^A is the attenuation quantization noise with variance given by (11), see Goldshtein et al. (2008) for details.

Let θ denote the required rain rate estimation at a specific location and $r_1,...,r_{N_\theta}$ a series of N_θ data point measurements from the nearby microwave links, located within a predetermined area, dependent on spatial correlation of rainfall and defined by the parameter q (radius of influence). The proposed model is based on the Inverse Distance Weighting (IDW) interpolation method (Shepard, 1968) over an irregular grid and its solution is given by:

$$\theta = \frac{\sum_{i=1}^{N_\theta}\left(W_i^{-1} + z\times\sigma_i^2\right)^{-1}\times r_i}{\sum_{i=1}^{N_\theta}\left(W_i^{-1} + z\times\sigma_i^2\right)^{-1}} \quad (15)$$

where W_i is the inverse squared distance weighting function. The dimensionless constant z and the radius of influence q [km] are determined experimentally, and for this study were taken 0.5 and 6 km, respectively. The unknown $r_{i,j}$, $i = 1,...,N$, $j = 1,...,K_i$ are obtained separately for each link $\hat{i} = 1,...,N$ according to the minimum MSE $\sum_{j=1}^{K_{\hat{i}}}\left(r_{\hat{i},j} - \hat{\theta}_{\hat{i},j}\right)^2$ between $r_{\hat{i},j}$, $j = 1,...,K_{\hat{i}}$ and the estimates of $\hat{\theta}_{\hat{i},j}$, calculated according to (15) at the locations of the $\hat{i}$ th link sample points from all other microwave links, excluding the link $\hat{i}$. The optimal $r_{\hat{i},j}$ are calculated in the way that preserves the total path-average rainfall, measured by the $\hat{i}$ th link**:** $\sum_{j=1}^{K_{\hat{i}}}\left(r_{\hat{i},j}\right)^{b_{\hat{i}}} = K_{\hat{i}}\left(R_{\hat{i}}\right)^{b_{\hat{i}}}$ (Goldshtein et al.**,** 2008). After adjusting all $r_{\hat{i},j}$ over the entire network, the procedure is iterated with new $r_{i,j}$.

The major advantage of this model over the EKF-advection is that it does not make any assumptions regarding the underlying physical model of the phenomena (besides spatial correlation of rainfall) ; the method can easily be adapted to various rainfall patterns or microwave networks since it requires tuning of only two parameters (*z* and *q*). The major disadvantage is that the procedure allows reconstructing rainfall fields in space, not in time.

b. Non-linear tomography

In the NLT technique, the area is divided into *M* cells which size varies in space and follows the local density of the microwave network (Figure 6). A system of *N* non-linear equations is formulated according to the assumption of constant rainfall intensity at each pixel:

$$\sum_{j=1}^{M} l_{ij} r_j^{b_i} - L_i R_i^{b_i} = 0, \; i=1 \ldots N \qquad (16)$$

The system of equations is then iteratively linearized and a linear inversion technique is employed at each iteration. Since the system (16) is in general underdetermined, a regularization operator (smoothing) is applied (Zinevich et al., 2008). The resulting estimates, related to the centers of the pixels then interpolated over the whole area using IDW (Shepard, 1968).

In general, both SHT and NLT algorithms make different but similar assumptions about the underlying physical model and are optimized with respect to the variable density of the microwave networks. NLT is better suited for the dense networks, where the assumption of constant rainfall over a pixel is valid, since it explicitly accounts for variations of rainfall intensity between different pixels along the link. However, it is a deterministic algorithm that does not assume any observation uncertainty. SHT is more appropriate for sparse networks, since the assumption of constant rainfall over a link segment is weaker than that of NLT; it explicitly accounts for the observation uncertainty. The EKF-based algorithm features advantages of both spatial techniques and incorporates the rainstorm dynamic analyses for better representing rainfall in data-void regions.

6. Case study: analyses and results

Figure 7 demonstrates four time slots showing the motion of a part of the front, reconstructed using EKF from the RSL records from microwave links, obtained at spatial and temporal resolution of 1.5x1.5 km^2 and 1 min, and corresponding radar images. The spatial resolution of radar is 0.775x0.775 km^2. The microwave map shows rainfall at the radar clutter area where the radar is unable to measure.

This qualitative comparison shows that in general microwave patterns follow those of the radar. The link L1 shows almost zero rainfall at 1533 LT 26 December 2006 (from now on, time stamps are taken from the microwave maps) that results from missed weak rainfalls due to 1 dB quantization of microwave observations. At 1539, microwave map shows strong rainfall in the middle of the map which demonstrates the ability of the spatio-temporal reconstruction technique to estimate rainfall in the data-void area (only L1 records a part of the front at that time). Due to simplicity of the advection model that does not account for development/decay of convective cells, the microwave rainfall estimates at the south-east part exceed those of the radar since at all four time frames (especially at 1554) the model continues to translate the rainstorm features exactly as they were "seen" by the links in the past.

At 1533, 1539 and 1545 a "false" front, mainly caused by the link L3 is observed prior to the major one; the reason for this effect is the lack of links besides L3 at the northern part of the map, so that it the algorithm misses the actual distribution of rainfall along L3, producing uniform rainfall along the link. Note zero rainfall near the link L13 at 1533; here, the 2.56 km link recorded 0.1 mm h^{-1} path-averaged rainfall. This indicates highly variable structure of the rainstorm (rainfall intensity in the surrounding pixels reaches 20 mm h^{-1}).

A convenient way to examine performance of the proposed technique is to apply linear regression to the EKF-reconstructed rainfall and rain gauge measurements. However, conventional linear regression fit assumes that the independent variable (rain gauge) is known with zero uncertainty. In our case, the algorithm estimates the average rainfall over a 1.5x1.5 km pixel while rain gauges provide only point measurements, which can be considered representing the average rainfall over the pixel area with some uncertainty. Therefore, the method of total least squares, assuming uncertainties in both independent and dependent variables (Krystek and Anton, 2007) was chosen as a more appropriate one. Note that the correlation between the Ramle West rain gauge and the Switch Ramle rain gauge that are located at the same reconstruction pixel reaches only 0.70 at the gauge separation distance of 1.5 km, which indicates the weak representativeness of point measurements for comparison and further justifies the necessity of total least squares.

The cumulative rainfall series obtained using microwave-based EKF-advection reconstruction has been compared to rain gauges at five different locations (see Figure 8). Three rain gauges out of five (Ramle West, Switch Ramle and Modi'in Shimshoni) are located in close proximity of microwave links (links cross the pixels, compared to rain gauges). Other rain gauges (Kfar Shmuel and Maccabim) are located away of microwave links; the ability of the algorithm to interpolate rainfall in space and time is assessed in these sites. The skills of the method (correlation coefficient, bias, RMSE and the linear regression equation) of the microwave-derived rainfall measurements vs. rain gauges measurements are given in Table 2 and analyzed in detail below.

a. Ramle West and Switch Ramle rain gauge stations

One can see that in the Ramle area (rain gauges Ramle West and Switch Ramle) the EKF- and NLT- derived estimates outperform SHT both in terms of correlation ρ and RMSE, since the density of links at this area is high. In this case, SHT effectively averages over the nearby links, providing the averaged areal rainfall which is inherently lower than the point rainfall, measured by rain gauges. For the same reason, the SHT measurements have a consistent negative bias over all five sites. The microwave measurements, assimilated into the dynamic model are able to track the short-term variations in rainfall intensity more accurately. In the EKF-based algorithm only microwave measurements which contributed in the past (according to the storm dynamics) into the estimation of rainfall rate at a specific point in time and space take part. The scatter plots (Figure 9) demonstrate the ability of the EKF-based reconstruction to better represent the temporal variability and especially high intensity peaks, that expresses in the slope coefficient of the regression equation closer to one (see Table 2).

The regression equation for Ramle West shows slope smaller than one (0.83) and intercept of 0.39. To get insight into the reasons behind, let us first compare the rain gauge with the closest bi-directional microwave links (L11 and L12). The resulting regression equations are given in Table 3.

It can be seen that the short (1.6 km) link L11, oriented nearly orthogonally to the rain front direction, shows very good agreement with Ramle West gauge; conversely, link L12 shows lower average rainfall as it averages over its length (6.56 km) oriented along the rain front movement direction; this is the reason for high intercept values (0.79, 1.08) since the link L12, being oriented orthogonally to front, records rainfall even at the time frames when the gauge does not.

Ideally, the EKF reconstruction could be able to track the rain front peak along the link L12 and the lower average rainfall in L12 would have a little effect on estimation at the Ramle West location; in practice, due to lack of the information about distribution of rainfall along the link L12, it provides lower estimates at the Ramle West location. As a result, all three reconstruction algorithms underestimate the high intensity peaks relatively to the point measurements by rain gauges at Ramle West (Figure 8 (A), Table 2; see also Figure 11 (A)).

Note that the intercept coefficients at the 1 minute resolution (Table 2) are slightly higher than zero (0.39 and 0.23); the same effect is observed at the Modi'in Shimshoni station (intercept of 0.41). It can be seen at Figure 9 (A, B, D) that in many cases microwave links record rainfall when rain gauges show no rainfall at all. This can be attributed to the spatial variability of rainfall, i.e. longer links, especially the ones oriented in parallel with the front record rainfall when the gauges do not. This difference diminishes, resulting in intercept coefficients -0.15, -0.17 and -0.04 at 10 minute accumulation (Figure 11).

b. Kfar Shmuel rain gauge station

Note that while Ramle West and Switch Ramle gauges are located directly near links, the Kfar Shmuel gauge is about 2.5 km from the nearest microwave link (L1). SHT and NLT in this case perform worse (ρ = 0.65 and 0.67 vs. ρ = 0.75 for EKF-based reconstruction) due to the temporal delay, necessary for a storm to reach from the link L1 to the Kfar Shmuel station. Accounting for the delay results in a temporal lag of 2 minutes; by artificially shifting the time series, derived from the SHT rain maps at the Kfar Shmuel station by 2 minutes, ρ rises from 0.65 to 0.77. However, EKF (and, similarly, NLT) shows prominent bias (overestimation) of 0.41 mm h^{-1} relatively to the gauge, expressing also in high linear regression slope coefficient (1.41), which is in agreement with the difference of 1.5 mm h^{-1} between path-average rainfall, observed by the link L1 and the Kfar Shmuel rain gauge for the whole 22-hours period. To understand the reasons behind this overestimation, let us compare the time series of hourly accumulated rainfall, recorded by the bi-directional link L1 and the rain gauge (Figure 10, A).

It can be seen that the link L1 provides higher rainfall intensities with respect to the rain gauge at the front arrival at about 0130 and 0730 LT 27 December 2006, which is most likely due to higher spatial variability of rainfall. The secondary convergence lines of the storm are less regular and are represented by sporadic convective cells showing less homogeneity than for example arrivals at 1530 LT 26 December 2006, see Figure 1 (B). For this reason, the link L1, oriented roughly in parallel with the fronts, is exposed to more convective cells than the point gauge, which results in the higher rain rates; rainfall peaks between 0142-0210 LT 27 December 2006 are completely missed by the rain gauge (Figure 10, B). Accordingly, it can be seen from Table 2 that during the whole event the average rain rate recorded by Kfar Shmuel rain gauge is 2.56 mm h^{-1} vs. about 3 mm h^{-1} for other four gauges. Note that SHT that averages over wider area including L2 produces lower rainfall at this site.

Another example of the discrepancy between link and gauge measurements is the rainfall peak at 1530 LT 26 December 2006 that is missed by the link L1 (Figure 10, C). At 1545, however, the link L1 again records a longer peak than that of the gauge.

Note that the link L1 misses weak rainfalls between front arrivals around 1700, 2200 (Figure 10, A), which is most likely due to 1 dB quantization of attenuation records (see Zinevich et al. (2008) for details).

c. Modi'in Shimshoni rain gauge station

In the Modi'in area, SHT and NLT perform similarly but slightly better than the EKF-based reconstruction. Thus, the correlation with the Modi'in Shimshoni rain gauge located directly on the links L8 and L9 for the SHT(NLT) reaches 0.81(0.80) vs. 0.77 for the EKF-based algorithm, and RMSE for spatial algorithms is 3.26(3.30) mm h^{-1} vs. 3.51 mm h^{-1} for EKF. Since the station is located in the close proximity of the links L8 and L9, the SHT estimate at this point is not distorted by rainstorm track affecting EKF and represents the path-averaged estimate of rain rate based on L8, L9 only. Figure 8 (D) shows that there is consistent underestimation of EKF-derived rainfall with respect to the rain gauge around 0000, 0130 0300 LT 27 December 2006, that can again be attributed to the spatial variations of rainfall (there are no confident estimates of rainstorm dynamic at those times that may indicate the sporadic character of the rainstorm); one can suggest that L7, L8 are roughly orthogonal to the advection direction. In this case, path-averaging effect of microwave links may result in underestimation of the rainfall, produced by isolated convective cells. As a result, EKF shows overall negative bias of -0.26 at the site of Modi'in Shimshoni; similarly, negative bias -0.21 and -0.29 are found in the SHT and NLT statistics (Table 2).

d. Maccabim rain gauge station

The rain gauge Maccabim is the most distant one, located 4 km from the nearest links (L7 and L8). Both EKF and spatial algorithms perform poorly at this site; however, EKF shows ρ =0.57 vs. 0.24 for SHT and RMSE 5.65 mm h^{-1} vs. 7.45 for NLT due to its ability to interpolate rainfall in both spatial and temporal dimensions. The EKF algorithm overestimates the rainfall at the Maccabim site from the beginning of the event until approximately 1800 LT 26 December 2006; cumulative rainfall, measured by link at this time reaches 24 mm – exactly the value, recorded by EKF at the Modi'in Shimshoni site during the same time frame, since EKF simply translates the rainfall field registered by L7, L8. The discrepancy between EKF results and the Maccabim rain gauge is most likely caused by decay of the front, which can also be seen at Figure 7, time slot 1554. The EKF algorithm starts to miss rainfall consistently at about 0300 LT 27 December 2006; there is no indication of exact rainstorm direction at that time since there were no prominent fronts tracked by the multitude of microwave links (Figure 5). The differences between microwave links and the gauge at the period of 0000-0300 time follows the same pattern as in the Modi'in Shimshoni station (Figure 8, E, D). At 0300-1000, the EKF algorithm misses a considerable amount of rainfall due to rainstorm direction change: it can be seen (Figure 2) that there are no nearby microwave links in front of the Maccabim site for the rainstorm, arriving from north-east at 0300-1000. At those times all three algorithms show negative bias of about -0.65 since there are no microwave links that record rainfall observed by the Maccabim rain gauge.

When artificially introducing a time lag of 5 minutes into the SHT reconstruction, the correlation at Maccabim raises from 0.23 up to 0.63 and RMSE lowers from 7.5 mm h^{-1} to 5.4 mm h^{-1}, since this operation compensates the time delay necessary for the storm to arrive from Modi'in to Maccabim. However, it should be noted that such temporal shift results in improvement mostly due to the similarity of different parts of the front with each other, since (as it follows from Figure 2), the only time frame when links L7, L8 observe the same part of the front as the Maccabim gauge is between 1930-0000 LT 26-27 December 2006 (the rainstorm azimuth is around 90-110°).

e. Accumulating over 10 minutes interval

Accumulating results over the 10 minutes interval diminishes the differences between the all three reconstruction algorithms, producing temporal correlations of up to 0.97 (see Table 4, Figure 11), lowering the timing errors of the spatial algorithms. The best RMSE 1.59, 1.62 and 3.87 mm h^{-1} are achieved by EKF for the Ramle West, Switch Ramle and Maccabim stations and the best RMSE of 2.35 and 1.35 mm h^{-1} at the other two stations are achieved by SHT. The linear regression slope coefficient of SHT at Ramle West, Switch Ramle and Kfar Shmuel stations is considerably lower than that of EKF or NLT (0.80-1.19 vs. 0.91-1.59), which arises from the missed high rain rates due to the SHT averaging effect. At the Maccabim site, the slope coefficient for EKF (0.56) is lower than that of SHT and NLT (0.65 and 0.60), which results from lowering of short periods of peak intensity during advection of rain fronts from L7,L8 to the Maccabim location. This smoothing effect of EKF advection can be seen that by comparing the EKF records at Figure 8 (D, E): for example, a clearly observable peak at 1500-1600 on Figure 8 (D) is smoothed after being translated to the Maccabim site (Figure 8, E).

7. Conclusion

The paper explored the concept of recovering the rainstorm dynamics from correlations of multiple commercial microwave communication links and assimilation of observations into a stochastic spatio-temporal rainstorm model, based on the rainstorm advection and the extended Kalman filter, through comparison of the microwave-derived rainfall estimates to five ground rain gauges. In addition, the spatio-temporal reconstruction results were compared to two spatial reconstruction techniques. All three algorithms show similar performance for three rain gauges, located in the close proximity to microwave links. The spatio-temporal EKF-based technique performs better than spatial algorithms when compared to two other rain gauges, located 2-4 km away of microwave links (correlations 0.75 vs. 0.67 and 0.57 vs. 0.24 at 1 minute temporal sampling) that demonstrates the ability of the method to capture the rainstorm dynamics (velocity and direction) and to track the rainstorm accordingly.

Measuring the near-surface areal distribution of rainfall at the temporal resolution of 1 minute is a unique advantage of the commercial microwave network used in this study; it is known that the sampling interval of 5 minutes, typical for radars, can be a considerable source of errors (Piccolo et al, 2005). In addition, the communication systems are constructed according to the long-term rainfall statistics in the local climate to assure minimum interruption in any weather conditions by providing enough fade margins for the strongest rainfalls occurring in the region.

The important meteorological benefits of measurements by commercial microwave links are accurate mapping of near-surface precipitation over wide areas, including currently unmapped areas (e.g. regions with complex orography), measurement of urban precipitation, where the high density of microwave links advantageously provide redundancy, and mapping of the horizontal wind field of a storm, similar to the mapping produced by Doppler radars.

However, much work still needs to be done to bring the approach to the operational level. Thus, representing rain front movement as a plane in the $\{\delta x, \delta y, \delta t\}$ space can be a valid assumption only over small areas. Next, only in the case of homogeneous rain front it is possible to correlate the same rainstorm features recorded by different links. This becomes problematic if a rainstorm is formed of sparse rainfall cells, as at 0130-0600 LT 26 December 2006 when no time frames were considered confident; the missed information can be taken from adjacent areas. The dynamic model in the present form does not allow real-time observations; forecasting advection dynamics and rainfall uncertainties (model error covariance) should be considered. The pure translation model accounting for neither diffusion nor development/decay of the individual rain cells is valid only over short time periods and small areas; a-priori diffusion coefficients may be introduced. The problem is generally underdetermined, since the number of links is limited; introducing spatial correlation into the model may be necessary. The problem of spatial scale of the model is essential: on one hand, pixel size should be small relatively to the typical size of a rain cell, to diminish the numerical diffusion and allow more accurate representation of the rainstorm features; on the other hand, pixel size is limited by the rainstorm velocity and numerical stability of the second order numerical scheme. Possible solutions may involve splitting each time step into a number of shorter steps so that the Courant numbers stay less then one, and introducing flux limiters to prevent oscillations of the solution. In the study, zero rainfall attenuation was determined from a-priori known dry periods immediately before the beginning of the event; in a real application, the changes of zero rainfall attenuation during an event due to variations in air moisture and scintillation effects should be taken into account. Finally, dense communication networks allowing observation at high temporal and spatial resolution, are not available everywhere; it was shown that the quality of reconstruction at every point depends on the availability of nearby links. Besides, the technique needs to be tested on rainfall patterns other than the frontal rainstorm, described here.

Acknowledgments.

We deeply thank O. Goldshtein and A. Rayitsfeld (Tel Aviv University), A. Shilo and E. Moshayov (Pelephone) for their cooperation in supplying microwave data and help in installation of rain gauges, and to Y. Levi (Mekorot) for the radar data. This research was funded in part by the Horowitz fund, the Porter School of Environmental Studies at Tel Aviv University and the GLOWA-Jordan River project funded by the BMBF, Germany and MOS, Israel. The authors are grateful to Hidde Leijnse and two anonymous reviewers for their valuable comments.

References

Allen, D., Douglas, A., Rood, R., Guthrie, P., 1991: Application of a monotonic upstream-biased transport scheme to three-dimensional constituent transport calculations. *Mon. Wea. Rev.,* **119**, 2456-2464.

Atlas, D., Ulbrich, C., 1974: The physical basis for attenuation-rainfall relationships and the measurements of rainfall parameters by combined attenuation and radar methods. *J. Rech. Atmos.,* **8**, 275-298.

Atlas, D., Ulbrich, C., 1977: Path- and area-integrated rainfall measurement by microwave attenuation in the 1-3 cm band. *J. Appl. Meteor.,* **16**, 1322-1331.

Berne, A., Uijlenhoet, R., 2007: Path-averaged rainfall estimation using microwave links: Uncertainty due to spatial rainfall variability. *Geophys. Res. Lett.*, **34(7),** L07403.

Daley, R., 1995: Estimating the wind field from chemical constituent observations: experiments with a one-dimensional extended Kalman filter. *Mon. Wea. Rev.*, **123,** 181-198.

Desa, M., Niemczynowicz, J., 1997: Dynamics of short rainfall storms in a small scale urban area in Coly Limper, Malaysia. *Atmos. Res.,* **44,** 293-315.

Drécourt J.-P., 2004: Data assimilation in hydrological modeling, *Ph. D. thesis.*

Giuli, D., Facheris, L., Tanelli, S., 1999: Microwave tomographic inversion technique based on stochastic approach for rainfall fields monitoring. *IEEE Trans. Geosci. Remote Sens.,* **37(5)**, 2536-2554.

Feingold, G. and Levin, Z., 1986: The lognormal fit to raindrop spectra from frontal convective clouds in Israel, *J. Appl. Meteor.,* **25**, 1346-1363.

Goldreich, Y., 2003: *The Climate of Israel: Observation, Research and Application*. Springer*,* 298 p.

Goldshtein, O., Messer, H., Zinevich, A., 2008: Rain rate estimation using measurements from commercial telecommunications links. *IEEE Trans. Signal Proces.,* in press.

Grum, M., Kraemer, S., Verworn, H., Redder, A., 2005: Combined use of point rain gauges, radar, microwave link and level measurements in urban hydrological modeling. *Atmos. Res.,* **77(1-4)**, 313-321.

Holt, A., Goddard, J. Upton, G.l, Willis, M. Rahimi, A., Baxter, P., Collier, C., 2000: Measurement of rainfall by dual-wavelength microwave attenuation. *Electronic Letters,* **36(25)**, 2099-2101.

Holt, A., Kuznetsov, G., Rahimi, A., 2003: Comparison of the use of dual-frequency and single-frequency attenuation for the measurement of path-averaged rainfall along a microwave links. *IEE Proc.-Micro. Antennas Propag.,* **150(5)**, 315-320.

Hourdin, F., Armengaud, A., 1999: The use of finite-volume methods for atmospheric advection of trace species. Part I: Test of general formulations in a general circulation model. *Mon. Wea. Rev.,* **127**, 822-837.

Jameson, A., 1991: A comparison of microwave techniques for measuring rainfall. *J. Appl. Meteor.,* **(30)**, p. 32-54

Jinno, K., Kawamura, A., Berdtsson, R., Larson, M., Niemczynowics, J., 1993: Real-time rainfall prediction at small space-time scales using a two-dimensional stochastic advection-diffusion model. *Water Resour. Res.*, **29**, 1489-1504.

Kawamura, A., Jinno, K., Berndtsson, R., Furukawa, T., 1997: Real-time tracking of convective rainfall properties using a two-dimensional advection-diffusion model. *J. Hydrol.*, **203**, 109-118.

Krämer, S., Verworn, H., Redder, A., 2005: Improvement of X-band radar rainfall estimates using a microwave link. *Atmos. Res.,* **77(1-4)**, 278-299.

Krystek, M., Anton, M., 2007: A weighted total least-squares algorithm for fitting a straight line, *Meas. Sci. Technol.*, **18**, 3438-3442.

Leijnse, H., Uijlenhoet, R., Stricker, J., 2007a: Rainfall measurement using radio links from cellular communication networks. *Water Resour. Res.,* **43(3),** W03201.

Leijnse, H., Uijlenhoet, R., Stricker, J., 2007b: Hydrometeorological application of a microwave link: 2. Precipitation. *Water Resour. Res.*, **43,** W04417.

Leijnse, H., Uijlenhoet, R., Stricker, J., 2008: Microwave link rainfall estimation: Effects of link length and frequency, temporal sampling, power resolution, and wet antenna attenuation, *Adv. Water Resour.*, in press, doi:10.1016/j.advwatres.2008.03.004.

Messer, H., Zinevich, A., Alpert, P., 2006: Environmental monitoring by microwave communication networks. *Science*, **312**, 713**.**

Minda H. and Nakamura, K., 2005: High temporal resolution path-average rain gauge with 50-GHz band microwave. *J. Atmos. Oceanic Technol.*, **22,** 165–179.

Mishchenko, M., 2000: Calculation of the amplitude matrix for a nonspherical particle in a fixed orientation. *Appl. Opt.,* **39(6)**, 1026-1031.

Mizutani, H., 1981: Movement and deformation prediction for pluvial distributions. *Proc. ICASSP'81*, **6**, 1022-1025.

Piccolo, F., Chirico, G.B., 2005: Sampling errors in rainfall measurements by weather radar. *Adv. Geosci.,* **2**, 151-155.

Rahimi, A., Holt, A., Upton, G., Cummings, R., 2003: The use of dual-frequency microwave links for measuring path-averaged rainfall. *J. Geophys. Res.,* **108(D14),** 4467**.**

Rahimi, A., Holt, A., Upton, G., 2006: Attenuation calibration of an X-band weather radar using a microwave link. *J. Atmos. Oceanic Technol*, **23(3)**, 295-405.

Rincon, R., Lang, R., 2002: Microwave link dual-wavelength measurements of path-averageattenuation for the estimation of drop size distributions and rainfall. *IEEE Trans. Geosci. Remote Sens.*, **40(4)**, 760-770.

Shepard, D., 1968: A two dimensional interpolation function for irregularly spaced data. *In Proceedings of the 1968 23rd ACM national conference*, 517-523.

Upton, G., 2002: A correlation-regression method for tracking rainstorms using rain-gauge data. *J. Hydrol.,* **261(1-4)**, 60-73.

Upton, G, Holt, A., Cummings, R., Rahimi, A., Goddard, J., 2005: Microwave links: the future of urban rainfall measurement? *Atmos. Res.,* **77(1-4)**, 300-312.

Upton, G., Cummings, R., Holt, A., 2007: Identification of melting snow using data from dual-frequency microwave links. *Microw. Antennas Propag.,* **1(2),** 282-288.

Wilson, J., Crook, N., Mueller, S., Sun, J., Dixon, M., 1998: Nowcasting thunderstorms: A status report, *Bull. Amer. Meter. Soc.,***79**, 2079-2099.

Zinevich, A., Alpert, P., Messer, H., 2008: Estimation of rainfall fields using commercial microwave communication networks of variable density. *Adv. Water Resour.*, in press, doi:10.1016/j.advwatres.2008.03.003

List of Figures

FIG. 5. Change of advection velocity (A) and azimuth (B) over 15 time slots (13 measured values) over the entire event, interpolated at 1 minute resolution.

FIG. 6. Voronoi chart showing the variable density grid consisting of 18 non-uniform pixels, used for NLT reconstruction; pixel centers are denoted by (□).

FIG. 7. The series of snapshots of rainfall field, reconstructed using the stochastic space-time model from microwave links (right), compared to the weather radar images (left), over the entire test site at 4 time slots. The standard radar maps do not cover the whole area because of the clutter, while the maps, reconstructed from microwave links are restricted to the area where measurements were available. The interval between successive radar scans is 3-4 min, so that radar images were aligned so that the time slot at the microwave map falls approximately in the middle of radar scanning interval (e.g. 1533 on microwave map vs. 1536 on radar map).

FIG. 8. Cumulative rainfall extracted from the instantaneous rainfall maps produced by EKF-advection reconstruction, compared to the rainfall measured by rain gauges at five locations.

FIG. 9. Scatter plots and corresponding linear regression equations of the reconstructed rainfall fields vs. rain gauges, for the EKF-advection reconstruction at 1 minute resolution.

FIG. 10. Comparison of hourly accumulated time series of path-averaged rainfall intensity of the bi-directional link L1 vs. Kfar Shmuel rain gauge (A) and comparison of the same links and the rain gauge over a 1.5 hour segment (B), (C). The L1 time series were shifted by 3 minutes to compensate for 2.5 km distance between the link and the rain gauge.

FIG. 11. Scatter plots and corresponding linear regression equations of the reconstructed rainfall fields vs. rain gauges, for the EKF-advection reconstruction at 10 minute resolution.

TABLE 1. Power-law equation coefficients used in the study.

Coefficients	18 GHz	22 GHz	23 GHz
a_k	0.0521	0.0828	0.0915
b_k	1.1153	1.0741	1.0651

TABLE 2. Correlation coefficients ρ, bias and RMSE and linear regression equation of the microwave rainfall estimates vs. rain gauges at the 1 minute temporal resolution for the EKF-advection, SHT and NLT algorithms.

Statistics \ Rain gauges		Ramle West	Switch Ramle	Kfar Shmuel	Modi'in Shimshoni	Maccabim
ρ	EKF	0.85	0.83	0.75	0.77	0.57
	SHT	0.78	0.81	0.65	0.81	0.24
	NLT	0.84	0.86	0.67	0.80	0.23
Bias	EKF	-0.19	0.04	0.41	-0.26	-0.61
	SHT	-0.24	-0.01	-0.14	-0.21	-0.58
	NLT	-0.39	-0.16	0.58	-0.29	-0.76
RMSE	EKF	4.24	4.11	4.33	3.51	5.65
	SHT	5.13	4.27	4.29	3.26	7.47
	NLT	4.44	3.72	5.04	3.30	7.45
y=ax+b	EKF	0.83x+0.39	0.94+0.23	1.41x-0.64	0.78x+0.41	0.42x+1.47
	SHT	0.58x+1.14	0.67x+0.99	1.06x-0.29	0.83x+0.30	0.33x+1.80
	NLT	0.74x+0.50	0.84x+0.34	1.54x-0.79	0.83x-0.21	0.29x+1.77
Aver. rain rate		3.28	3.06	2.56	2.99	3.56

TABLE 3. Linear regression equations for the Ramle West rain gauge vs. its nearby bi-directional links L11 and L12.

Links	Forward direction	Backward direction
L11	0.97x-0.29	0.94x+0.03
L12	0.58x+0.79	0.56x+1.08

TABLE 4. Correlation coefficients ρ, RMSE and linear regression equations of the rainfall estimates vs. rain gauges at the 10 minutes temporal resolution for the EKF-advection, SHT and NLT algorithms.

Statistics \ Rain gauges		Ramle West	Switch Ramle	Kfar Shmuel	Modi'in Shimshoni	Maccabim
ρ	EKF	0.96	0.96	0.85	0.93	0.56
	SHT	0.95	0.94	0.84	0.94	0.58
	NLT	0.96	0.97	0.85	0.94	0.56
RMSE	EKF	1.59	1.62	3.04	1.54	3.78
	SHT	1.96	1.90	2.35	1.35	4.34
	NLT	1.79	1.36	3.11	1.36	4.42
y=ax+b	EKF	0.99x-0.15	1.07x-0.17	1.57x-1.05	0.93x-0.04	0.56x+0.95
	SHT	0.80x+0.40	0.87x+0.40	1.19x-0.63	0.95x-0.07	0.65x+0.68
	NLT	0.91x-0.07	0.98x-0.09	1.59x-0.93	0.94x-0.12	0.60x+0.65

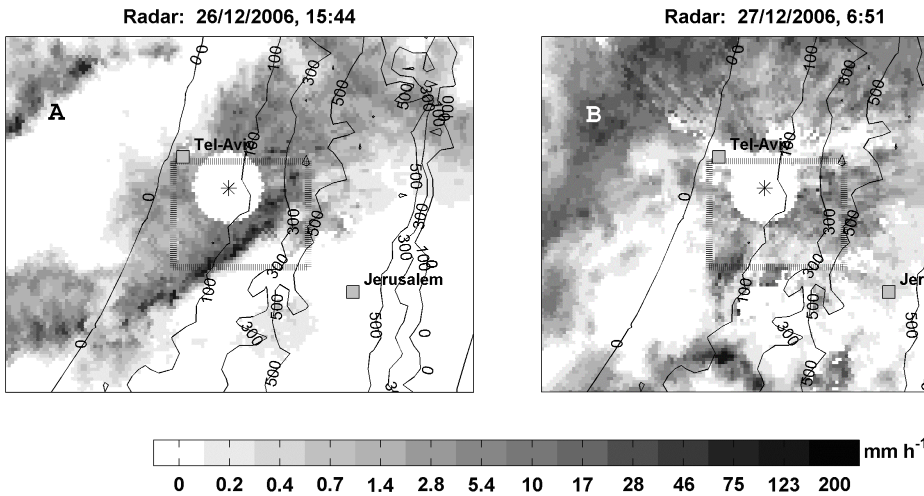

FIG. 1. Examples of radar maps of the studied event, showing (A) an arch-like rainstorm front moving from north-west and (B) sporadic convective cells 15 hours later. The studied area is marked by a rectangle.

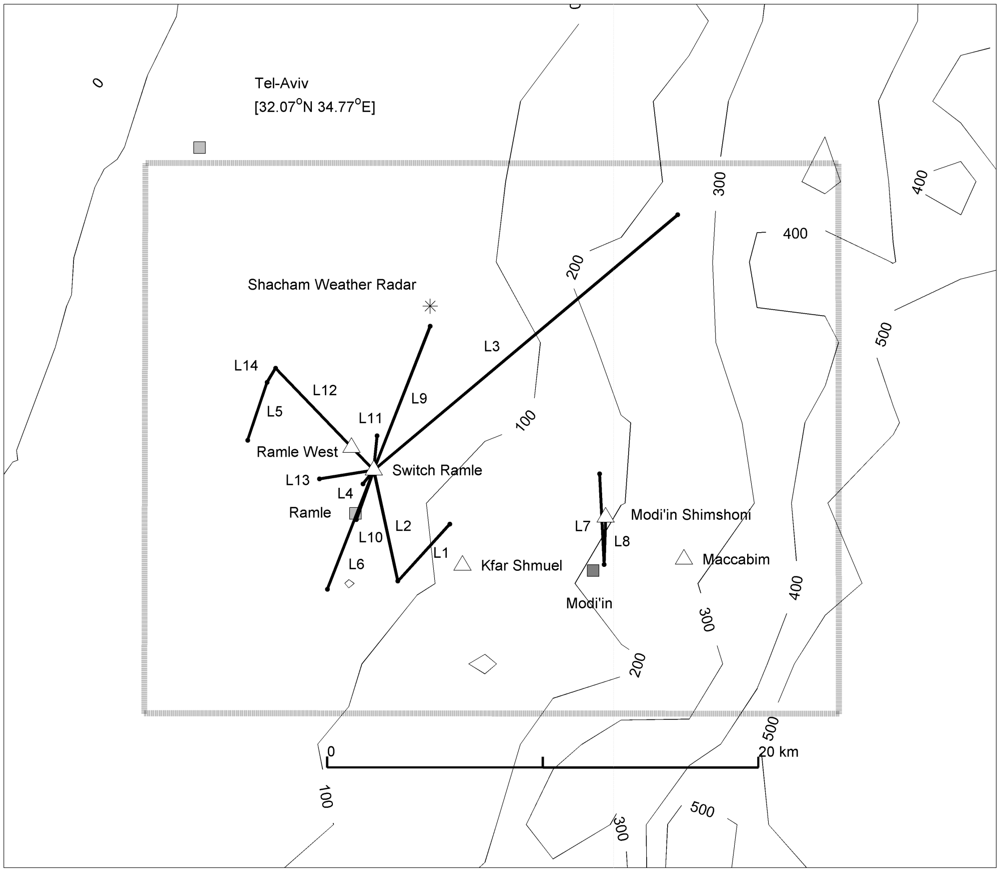

FIG. 2. Locations of microwave links, used for rainfall observations, around the cities of Ramle and Modi'in (□), rain gauges (Δ) Ramle West, Switch Ramle, Kfar Shmuel, Modi'in Shimshoni, Maccabim and the location of the weather radar (*). Out of 23 microwave links, 14 are distinct ones and other 9 complement some of them in opposite directions. The local orography contours are given in meters; height difference between the cities of Ramle and Modi'in is about 250 m. The surroundings of the cities are suburbs with low population density.

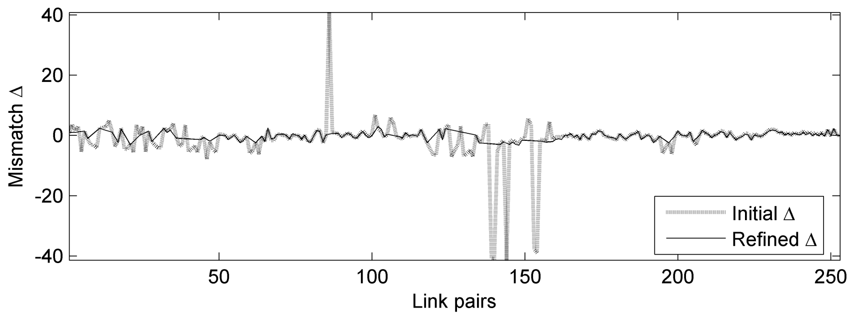

FIG. 3. Distribution of initial Δ_{ij} and refined $\widetilde{\Delta}_{ij}$ for 253 and (after removing outliers) 189 different pairs of links at the time slot 1930 – 2230 LT 26 December 2006.

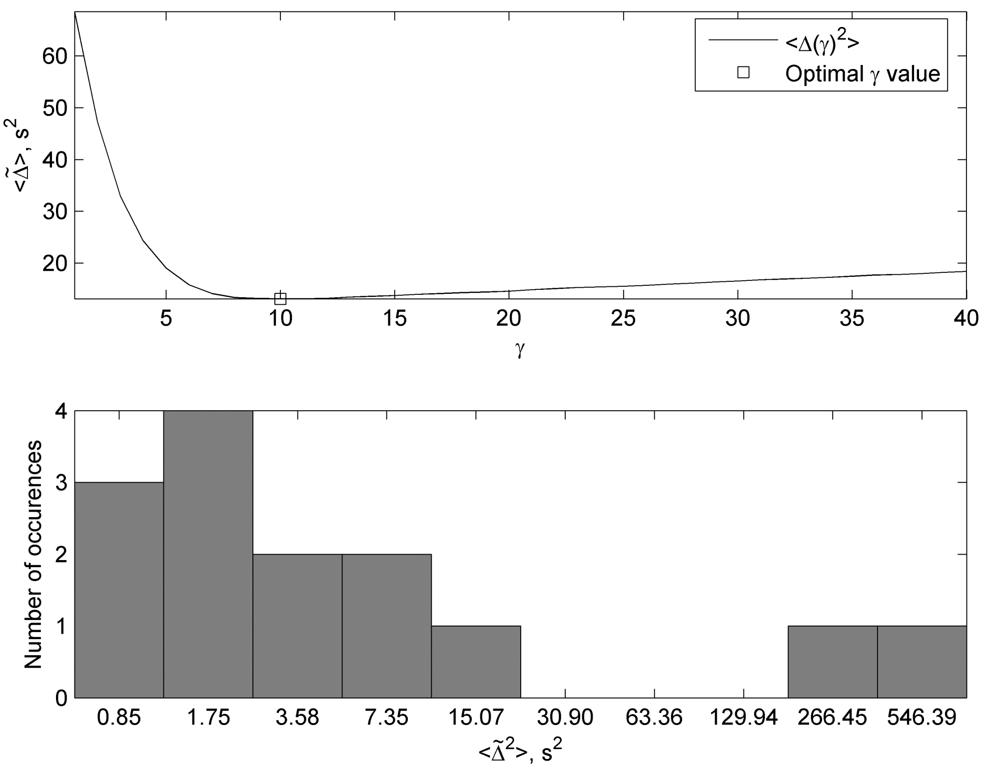

FIG. 4. Average mismatch $\left\langle \tilde{\Delta}(\gamma)^2 \right\rangle$ for different values of γ for the entire event (A) and a histogram of $\left\langle \tilde{\Delta}^2 \right\rangle$ for 14 time slots of the entire event under study (B). Time frames with large $\left\langle \tilde{\Delta}^2 \right\rangle$ correspond to the cases where it is impossible to determine rainstorm dynamics (no clear rainstorm features captured by the majority of the links).

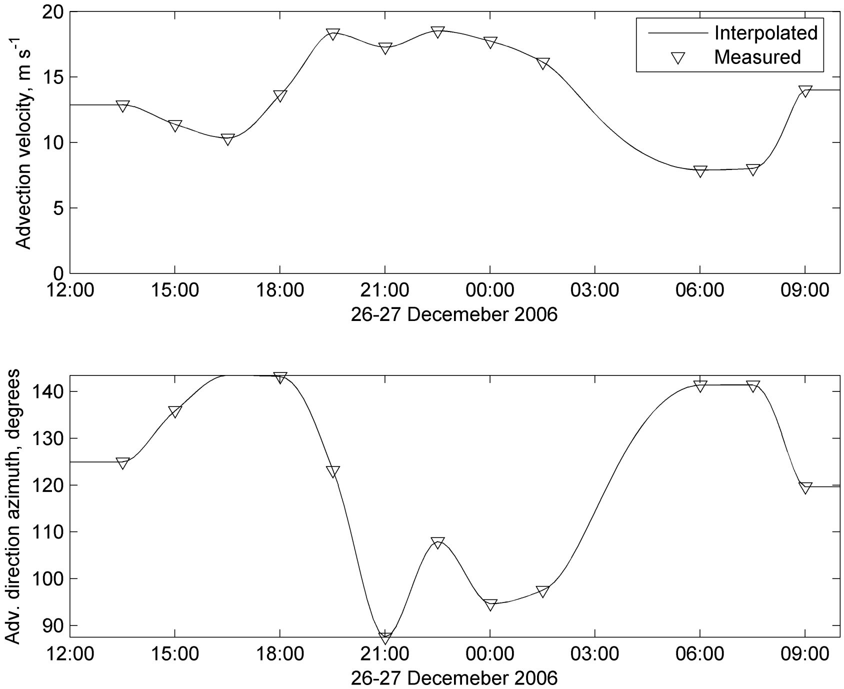

FIG. 5. Change of advection velocity (A) and azimuth (B) over 15 time slots (13 measured values) over the entire event, interpolated at 1 minute resolution.

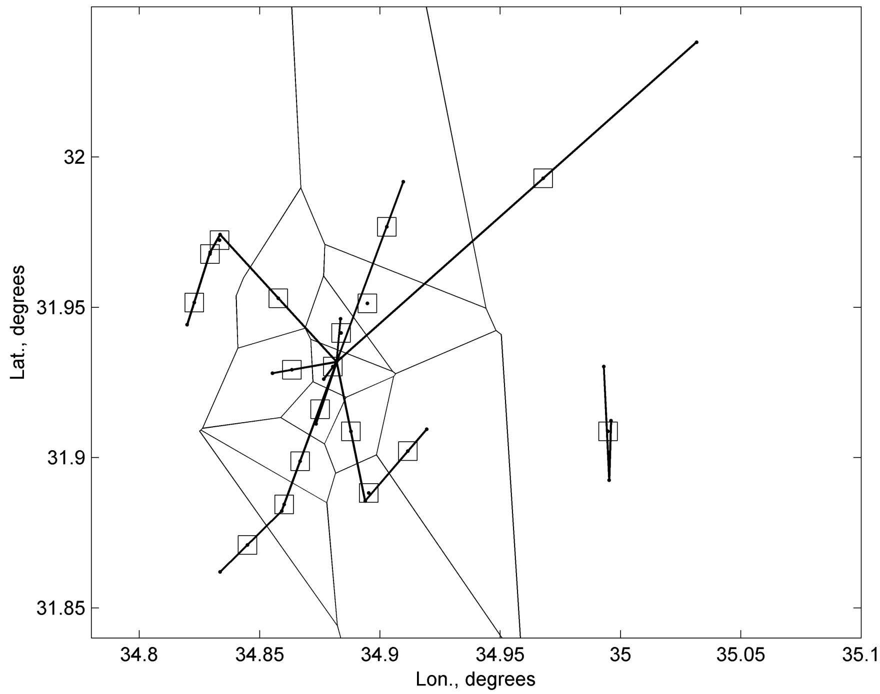

FIG. 6. Voronoi chart showing the variable density grid consisting of 18 non-uniform pixels, used for NLT reconstruction; pixel centers are denoted by (□).

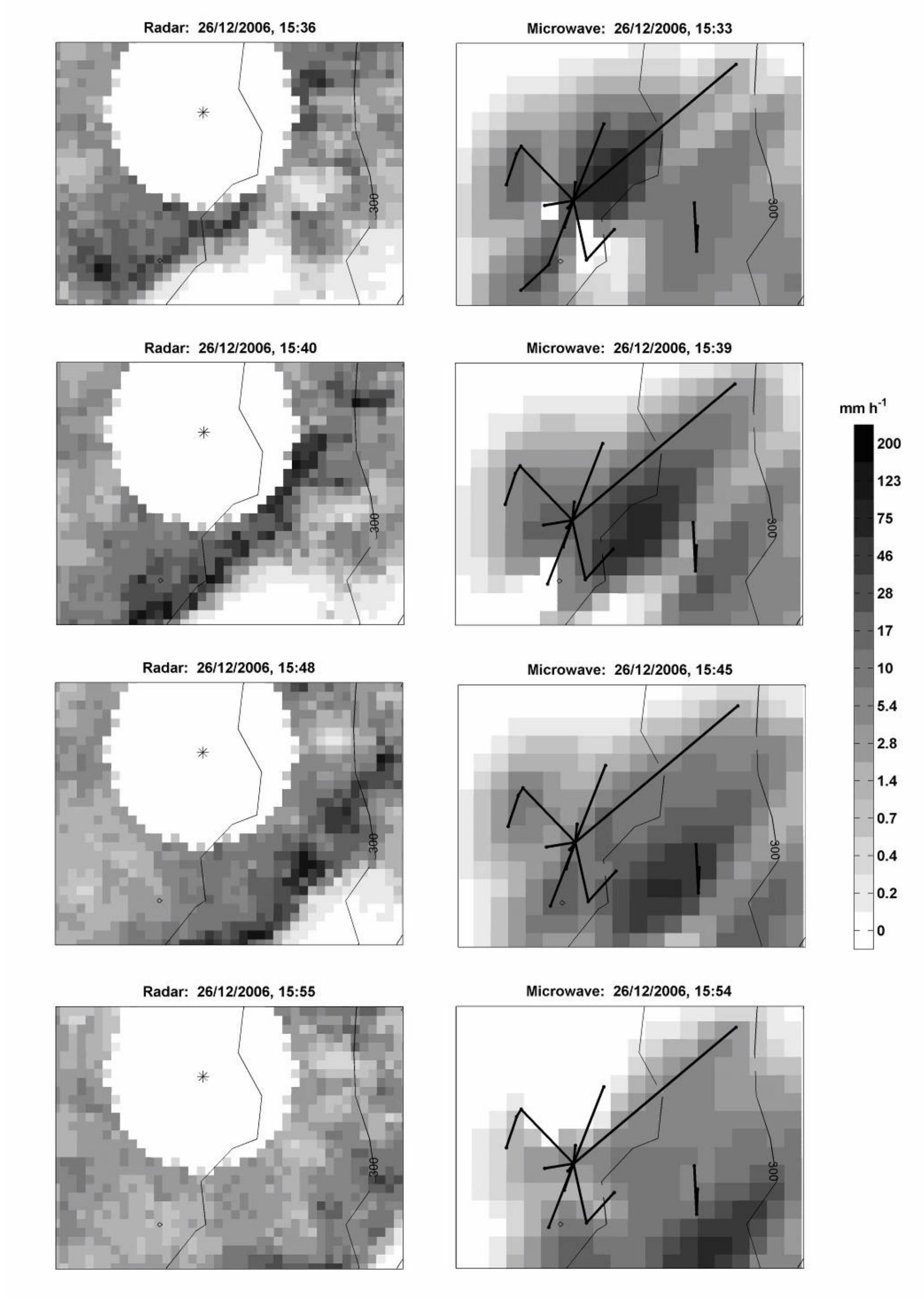

FIG. 7. The series of snapshots of rainfall field, reconstructed using the stochastic space-time model from microwave links (right), compared to the weather radar images (left), over the entire test site at 4 time slots. The standard radar maps do not cover the whole area because of the clutter, while the maps, reconstructed from microwave links are

restricted to the area where measurements were available. The interval between successive radar scans is 3-4 min, so that radar images were aligned so that the time slot at the microwave map falls approximately in the middle of radar scanning interval (e.g. 1533 on microwave map vs. 1536 on radar map).

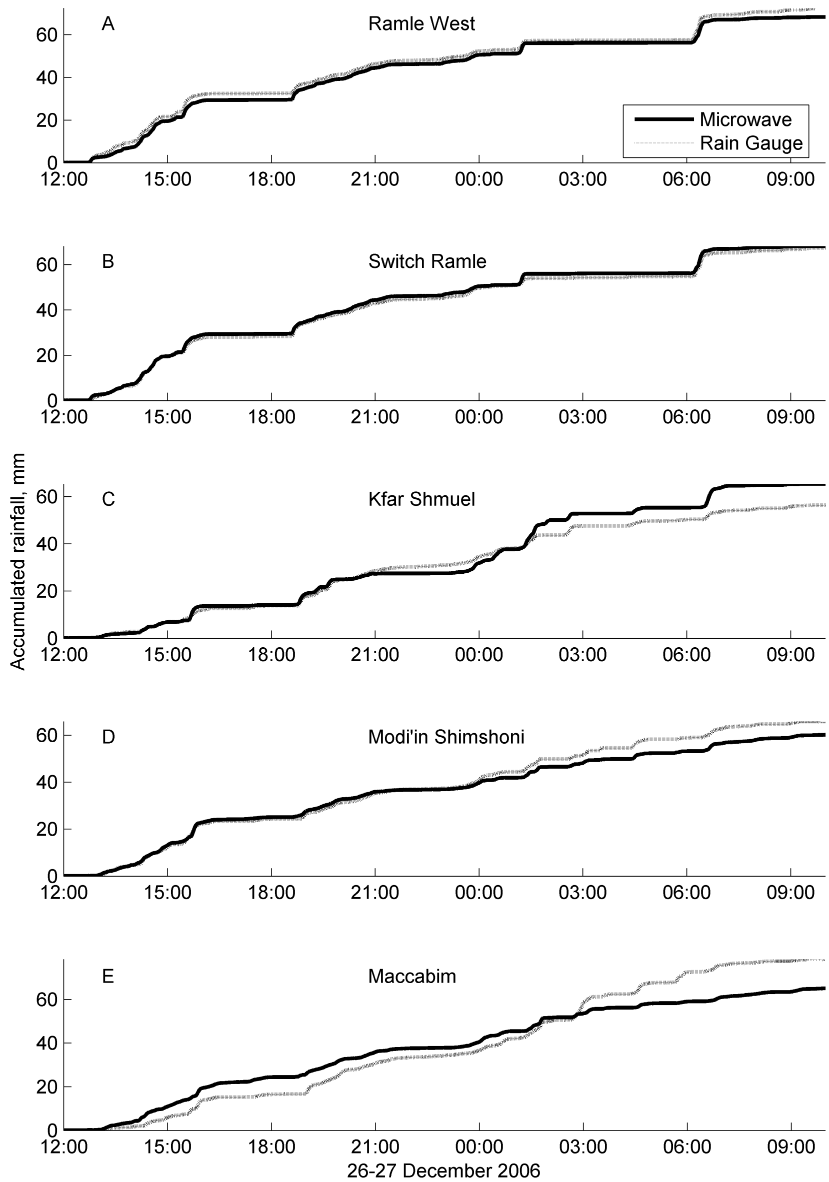

FIG. 8. Cumulative rainfall extracted from the instantaneous rainfall maps produced by EKF-advection reconstruction, compared to the rainfall measured by rain gauges at five locations.

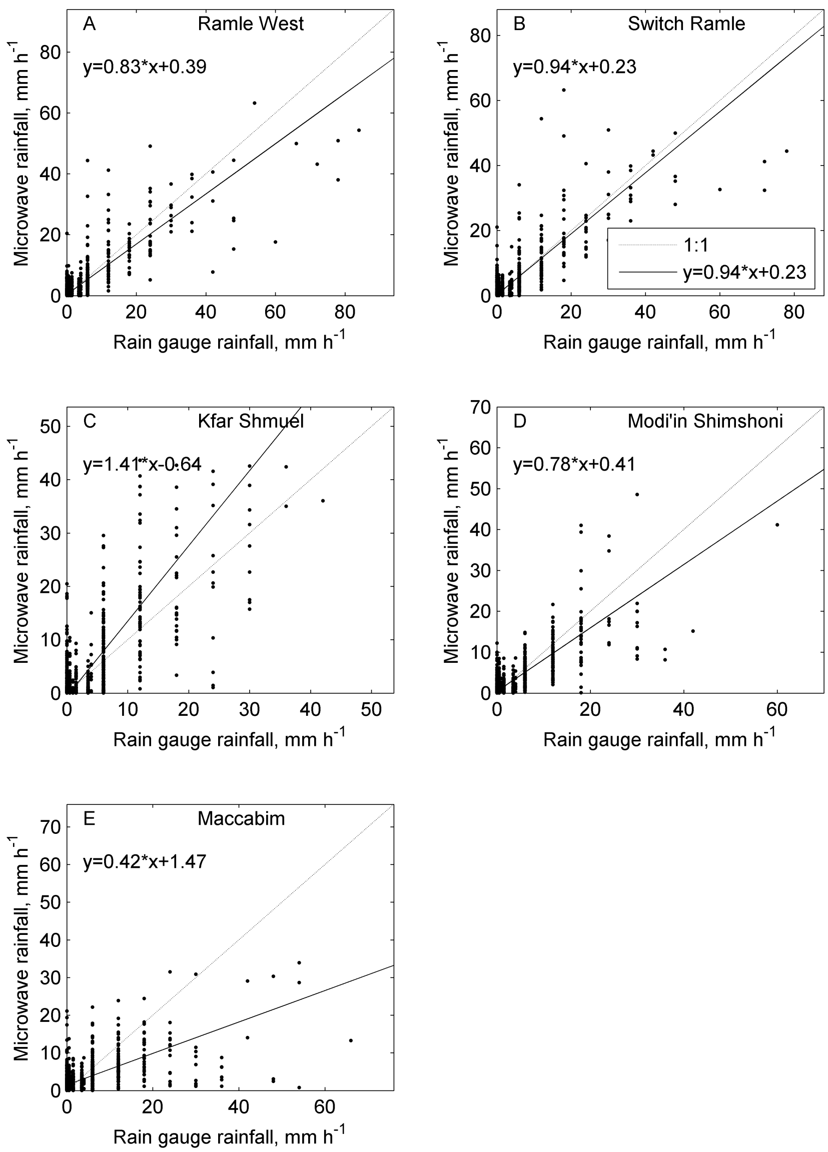

FIG. 9. Scatter plots and corresponding linear regression equations of the reconstructed rainfall fields vs. rain gauges, for the EKF-advection reconstruction at 1 minute resolution.

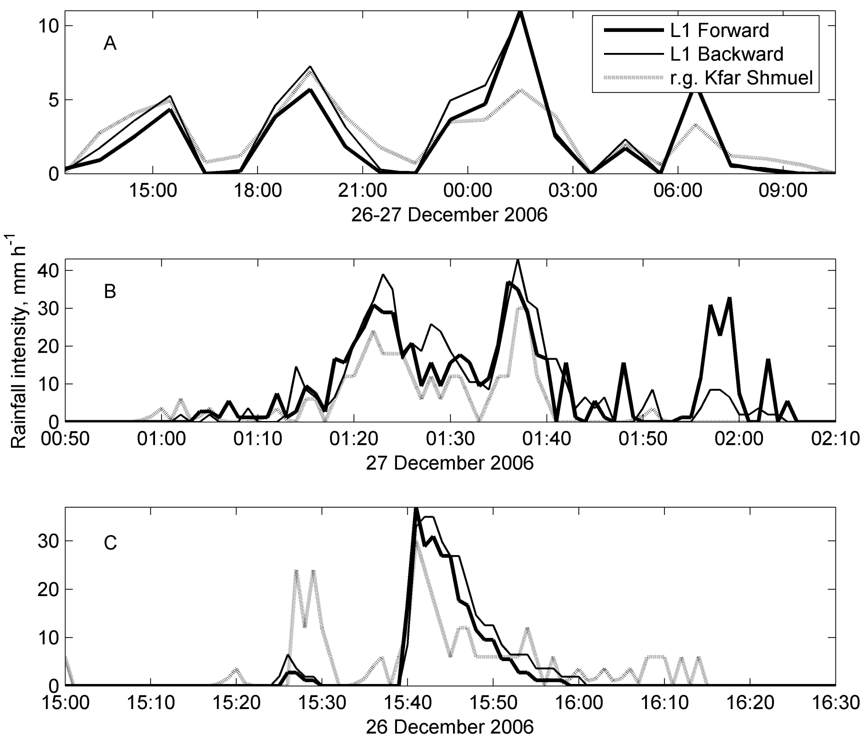

FIG. 10. Comparison of hourly accumulated time series of path-averaged rainfall intensity of the bi-directional link L1 vs. Kfar Shmuel rain gauge (A) and comparison of the same links and the rain gauge over a 1.5 hour segment (B), (C). The L1 time series were shifted by 3 minutes to compensate for 2.5 km distance between the link and the rain gauge.

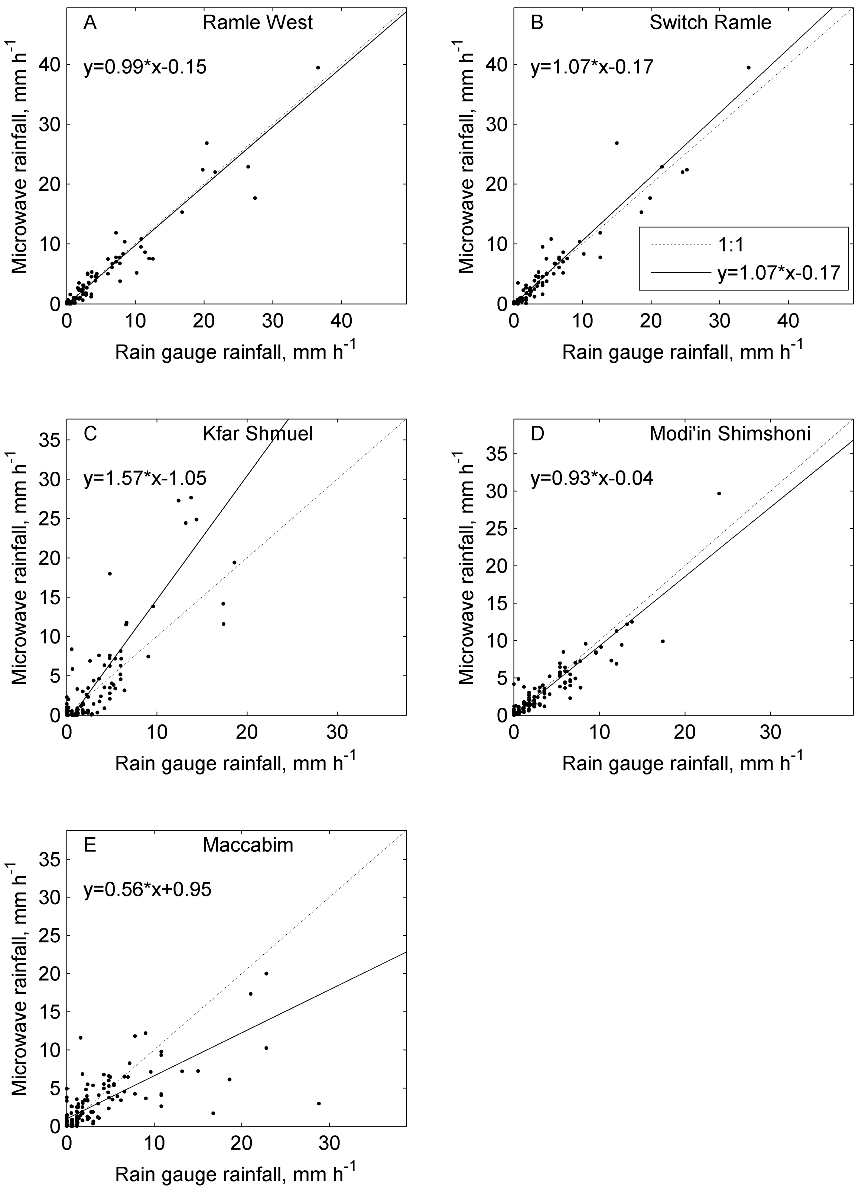

FIG. 11. Scatter plots and corresponding linear regression equations of the reconstructed rainfall fields vs. rain gauges, for the EKF-advection reconstruction at 10 minute resolution.